A&A, 715, A45 (2026)
https://doi.org/10.1051/0004-6361/202661734
© The Authors 2026

Astronomy & Astrophysics

Magnetic signatures in merger products

N. Muntean[1,⋆], L. Bugnet[1], L. Buchele[1], D. Dutta[1], L. Einramhof[1], P. G. Beck[2,3], L. Barrault[1], and B. Liagre[4]

[1] Institute of Science and Technology Austria (ISTA), Am Campus 1, Klosterneuburg, Austria
[2] Instituto de Astrofísica de Canarias, E-38200 La Laguna, Tenerife, Spain
[3] Departamento de Astrofísica, Universidad de La Laguna, E-38206 La Laguna, Tenerife, Spain
[4] Université Paris Cité, Université Paris-Saclay, CEA, CNRS, AIM, F-91191 Gif-sur-Yvette, France

Received 30 June 2026 / Accepted 6 September 2026

ABSTRACT

Asteroseismic estimates of the magnetic field strength in the radiative interior of red giant stars depend strongly on the internal stellar structure derived from models. Since red-giant-branch merger products have been shown to be able to possess a different core structure than single stars of the same mass, we investigated how a mass-gain history influences our estimates of an internal magnetic field strength. We constructed stellar models with and without a mass-gain event after the onset of the red giant branch evolutionary phase with masses of $1.1\,M_\odot \leq M \leq 2\,M_\odot$. First, by assuming a weak magnetic field, we investigated the influence of a mass-gain event on the global sensitivity of the oscillation frequencies to the magnetic field. We find that mass-gain models can be several times more sensitive to the field than single-star models of identical total mass at masses above $1.6\,M_\odot$. Therefore, considering a mass-gain evolutionary history for merger candidates allows a significant correction to the magnetic field strength. In the presence of strong magnetic fields, we also show that the critical field strength needed to suppress mixed dipole modes is significantly lower if a mass-gain event has occurred (for stars with masses of $M \gtrsim 1.6\,M_\odot$). The massive end of the suppressed stars' distribution is therefore strongly favored by a merger origin. We conclude that properly constraining the stellar evolutionary history is essential when aiming to constrain internal field strength estimates from asteroseismic observations.

Key words. asteroseismology – magnetic fields – binaries: general – stars: oscillations – stars: solar-type

1. Introduction

The internal processes of stars spanning a large variety of masses and evolutionary stages can be measured through the observation of their oscillations (e.g., Aerts et al. 2010) thanks to the data provided by missions such as CoRoT, *Kepler,* and TESS (Fridlund et al. 2006; Borucki et al. 2010; Ricker et al. 2015). The detection of mixed dipole oscillation modes in stars showing solar-like oscillations (e.g., Beck et al. 2011; Bedding et al. 2011; Mosser et al. 2011) and their frequency splitting due to rotation allowed for a direct constraint of the core rotation rate of stars on the red giant branch (RGB; Beck et al. 2012; Mosser et al. 2015; Vrard et al. 2016; Mosser et al. 2017, 2018; Tayar et al. 2019; Kuszlewicz et al. 2023) and in the subgiant phase (Deheuvels et al. 2012, 2014, 2016; Di Mauro et al. 2018; Deheuvels et al. 2020). The measurements revealed that the difference between the core and surface rotation of the studied stars was lower than predicted by standard hydrodynamic processes (e.g., Beck et al. 2012; Ceillier et al. 2017). This discrepancy suggests that there are additional angular momentum processes not accounted for in current models.

Besides rotation, internal magnetic fields directly affect angular momentum and chemical transport (Goode & Thompson 1992; Thompson et al. 1996; Mestel et al. 1988; Takahashi & Langer 2021). These internal magnetic fields can be probed by seismology, as they have a perturbing effect on stellar oscillations (e.g., Gough & Thompson 1990). Thus, the inclusion of magnetic effects in purely hydrodynamic processes proves to be one of the most promising paths to fully understand the rotational measurements found for RGB stars.

The first observational evidence for possible magnetic fields in the interior of RGB stars came in the form of suppressed dipole modes (Mosser et al. 2012; García et al. 2014). It was proposed by Fuller et al. (2015) that the mode suppression stems from a trapping of the oscillation energy in the stellar core by a magnetic field. Subsequent studies (Stello et al. 2016a,b) showed that suppressed dipole modes are common in red giants (RGs) that are massive enough to have possessed a convective core during the main sequence (MS). An explanation of the core fields required to obtain such suppression effects is offered by the fossil field scenario, in which the magnetic field present during the RGB phase of a solar-like oscillator is assumed to be a remnant field created by the convective motions in the core during its MS phase (e.g., Cantiello et al. 2016; Bugnet et al. 2021).

Past studies on the effect of magnetism on gravity-dominated mixed modes for magnetic fields that are too weak to cause dipole mode suppression show that a present internal magnetic field introduces a frequency shift to the gravity modes, which depends on their eigenfrequency (e.g., Gomes & Lopes 2020; Bugnet et al. 2021; Mathis et al. 2021; Loi & Papaloizou 2020; Loi 2021; Bhattacharya et al. 2024). This frequency shift causes a biased measurement of the pure dipole gravity mode period spacing ($\Delta\Pi_1$) that undershoots the true value, suggesting that magnetic fields are detectable and their strength measurable through asteroseismology (Loi 2021; Bugnet 2022; Deheuvels et al. 2023). By successfully measuring magnetic frequency shifts, multiple studies reported an estimation of the weighted average of the radial magnetic

⋆ Corresponding author: nico.muntean.nm@gmail.com

Open Access article, published by EDP Sciences, under the terms of the Creative Commons Attribution License (https://creativecommons.org/licenses/by/4.0), which permits unrestricted use, distribution, and reproduction in any medium, provided the original work is properly cited.
This article is published in open access under the Subscribe to Open model. Subscribe to A&A to support open access publication.

field strength $\langle B_r^2 \rangle^{1/2}$ (see Eq. (6)) for low-mass RGs (e.g., Li et al. 2022; Deheuvels et al. 2023; Li et al. 2023; Hatt et al. 2024; Villate et al. 2026). Theoretical works further provided tools to better constrain the magnetic field geometry expected in stellar cores (e.g., Mathis & Bugnet 2023; Das et al. 2024; Bhattacharya et al. 2024).

Previous works performed on magnetic detections implicitly assumed stellar models that follow a standard single-star evolution in their analysis. However, a growing body of evidence suggests that many RGB stars may instead be products of merger or mass-accretion events. In particular, the studies of Kochanek et al. (2014) and de Mink et al. (2014) showed that merger events are very common, with a predicted galactic occurrence rate of $0.2\,\mathrm{yr}^{-1}$, and that approximately 30% of high-mass MS stars can be classified as merger products. Synthetic population studies including Dvoráková et al. (2024) further suggest that merger events leading to low- to intermediate-mass remnants should also be a common occurrence. Recent asteroseismic studies (e.g., Rui & Fuller 2021; Deheuvels et al. 2022) report that a sizable number of *Kepler* giants show asteroseismic signatures consistent with a past merger or mass-accretion event. Indirect evidence of stellar mergers in the low- to intermediate mass range was provided by Beck (2026), whose authors demonstrate a significant reduction of the binary rate along the RGB as orbits shorter than $P_{\rm orb} \lesssim 1000$ days do not provide sufficiently large semi-major axes to allow the giant primary to complete their H-shell-burning phase without substantial star–star interaction, mass exchange, or common-envelope phases.

In a seismic context, previous works have focused on the products of stellar merger or accretion events that take place during and after the MS phase of the primary (e.g., Rui & Fuller 2021; Deheuvels et al. 2022; Henneco et al. 2024; Patton et al. 2025; Wu et al. 2026). The scenario of a stellar merger product produced by the merging of an RG possessing an electron-degenerate core and an MS star, both being of low- to intermediate-mass, was studied by Rui & Fuller (2021) and Deheuvels et al. (2022). The authors found that if the core structure of the RG is roughly conserved in the merger remnant, unusually low values for $\Delta\Pi_1$ are expected compared to single stars with similar $\Delta\nu$. While the possible effect of stellar merger events on magnetic field detection has been partially addressed (Villate et al. 2026), it requires new efforts for a more in-depth characterization. A merging or mass-gain event could have two possible effects: a change to the magnetic field itself or a change in the sensitivity of stellar oscillations to the field. In this work, we focused on the latter.

This work is aimed at studying the influence of a radiative interior-confined magnetic field on the properties of stellar oscillations of merger remnants. We assumed an axisymmetric dipole field for low- to intermediate-mass RGB stars that subsequently experienced a mass-gain or merger event. We introduce our stellar models in Sect. 2. In Sect. 3, we study how the inferred weighted average of the radial field strength behaves in the case of a weak field when comparing single-star and mass-gain models with identical masses, mode frequencies, and magnetic frequency shifts. Finally, in Sect. 4, we study how the minimum critical field strength is influenced by an assumed mass-gain or merger event in the case of a field strong enough to cause the suppression of the gravity component of dipole mixed modes. Throughout this paper, we refer to any event that increased the mass of our models as a mass-gain event, treating a stellar merger between an RGB and an MS as a specific instance of a mass-gain event.

2. Stellar models

In this study, we considered two classes of stellar evolutionary tracks: those evolved as single stars and those that experience a mass-gain event. We simulated the mass-gain event on the early RGB, by which point the cores of the stellar models had become degenerate. The fact that our models possess a degenerate core before the onset of the mass-gain event is essential, as it results in the core structure being broadly conserved during the mass-gain event (Rui & Fuller 2021). If the mass-gain event is considered at an earlier evolutionary stage, for example during the MS, the nondegenerate model core is able to readjust to the added mass in the envelope. This leads to the mass-gain model being indistinguishable from a single-star model of identical mass (see Figure 4 in Rui & Fuller 2021). All models were computed using the MESA stellar evolutionary code version 24.08.1, assuming an initial metallicity of $Z = 0.02$ and no rotation. For a summary of the assumed model physics, we refer the reader to Appendix A.1[1] (Paxton et al. 2011, 2013, 2015, 2019; Jermyn et al. 2023). We summarize the masses of our various models in Table 1 and provide more details below and in Appendix A.2.

2.1. Single stars

Our single-star grid spans initial masses from $1.1\,M_\odot$ to $2.0\,M_\odot$ in mass steps of $0.1\,M_\odot$. This is the typical mass range of red giant stars with detected internal magnetic fields (Li et al. 2022; Deheuvels et al. 2023; Li et al. 2023; Hatt et al. 2024; Villate et al. 2026; Deheuvels et al. 2026).

2.2. Mass gainers

The stellar models of the mass-gain model possess initial masses of $1.0\,M_\odot$, $1.5\,M_\odot$, and $1.6\,M_\odot$. The chosen initial masses allow us to study both low-mass progenitors and progenitors close to the transition mass ($\sim 1.5\,M_\odot$), where the behavior of the magnetic diagnostic changes as discussed in Sect. 3. We simulated a mass-gain event once the stellar model reaches the RGB, using the mass-accretion functionality of MESA. To ensure that the star was fully on the RGB, the mass-gain event was initiated once the model $\nu_{\rm max}$ decreased below a threshold value of $\nu_{\rm max,thr} = 250\,\mu$Hz (see Fig. A.1). The accreted material is of identical composition to the model envelope. This choice was motivated by the assumption that both stellar components that partake in a mass transfer/merger event must be formed in the same region of space, leading to minimal differences in envelope parameters such as metallicity.

The $M_{\rm init} = 1.0\,M_\odot$ models gained between 0.1 and $1.0\,M_\odot$, while the $M_{\rm init} = 1.5\,M_\odot$ and $M_{\rm init} = 1.6\,M_\odot$ models gained between 0.1 and $0.5\,M_\odot$ and 0.1 and $0.4\,M_\odot$, respectively. In the case of all initial masses, the total gained mass was varied in steps of $0.1\,M_\odot$. During the mass-gain event, we added $10^{-5}\,M_\odot/\mathrm{yr}$ to model a rapid accretion event following Rui & Fuller (2021). To avoid obtaining post-gain masses above the intended threshold, we constrained the simulation time step during the mass-gain event's duration to 250 yr/step. After the cessation of the mass-gain event, we continued to evolve the resulting mass-gain products according to standard stellar evolution.

[1] The MESA inlist file templates of our models are available on Zenodo: doi.org/10.5281/zenodo.23364968

Table 1. Mass properties of our representative stellar models.

Group	Model Type	$M_{\rm init}$ $[M_\odot]$	$M_{\rm total}$ $[M_\odot]$
[a]	single ●	1.1	1.1
	mass-gain ■	1.0	
[b]	single ●	1.4	1.4
	mass-gain ■	1.0	
[c]	single ●	1.6	1.6
	mass-gain ■	1.0	
	mass-gain ▲	1.5	
[d]	single ●	2.0	2.0
	mass-gain ■	1.0	
	mass-gain ▲	1.5	
	mass-gain ⬟	1.6	

Notes. The $M_{\rm init}$ and $M_{\rm total}$ columns represent the initial mass of the model and the model mass at the asteroseismic analysis ($\nu_{\rm max}$ = 180 μHz), respectively, while the group column represents the labeling in later plots for single-star and mass-gain models of identical $M_{\rm total}$.

For each single-star model in our grid, we computed at least one mass-gain model of equal total post-mass-gain mass. We find that the envelope conditions (in particular the effective temperature, $T_{\rm eff}$, and model radius, R) are very similar for single-star and mass-gain models of identical total masses. We provide a comparison of R and $T_{\rm eff}$ we obtained for the single-star and mass-gain models in Table A.1. We extracted a stellar profile from each of the models described above at a value of $\nu_{\rm max}$ = 180 μHz, a representative frequency at which magnetic signatures are commonly detected (e.g., Hatt et al. 2024).

3. Influence of mass-gain events on the signature of weak magnetic fields

We began by investigating how a mass-gain event impacts the influence of a weak magnetic field on stellar oscillations. The magnetic fields we considered are strong enough to induce a measurable frequency shift in g-dominated dipole mixed modes near $\nu_{\rm max}$ of our models (Bugnet et al. 2021), but too weak to cause dipole mode suppression (see Sect. 4, Fuller et al. 2015, and Stello et al. 2016b). In the following section, we briefly present the definition and meaning of the magnetic seismic parameters used in this part of the study.

3.1. Frequency perturbation due to weak magnetic effects

Internal magnetic fields perturb stellar oscillation frequencies, producing a measurable frequency shift of $\delta\nu_{\rm mag}$ (Das et al. 2020; Bugnet et al. 2021; Li et al. 2022). When only considering g-modes of high radial order, n, in the asymptotic regime (e.g., Unno et al. 1989), it was shown (see Hasan et al. 2005; Rashba et al. 2007; Bugnet et al. 2021) that the radial part of the magnetic field dominates the total influence on the frequency shift, $\delta\nu_{\rm mag}$. The frequency shift can then be expressed as (Li et al. 2022)

$$\delta\nu_{\rm mag} = \frac{\mathcal{I}}{(2\pi)^4\,\mu_0\nu^3}\int_{r_{\rm i}}^{r_{\rm o}} K(r)\overline{B_r}(r)^2\,{\rm d}r, \tag{1}$$

as long as the field has a significant radial component, B_r (Mathis et al. 2021; Bhattacharya et al. 2024). In Eq. (1), μ_0 is the vacuum permeability and $r_{\rm i}$ and $r_{\rm o}$ are the inner and outer boundaries of the g-mode cavity, respectively; the parameters $\mathcal{I}$, ν, and $\delta\nu_{\rm mag}$ are defined and discussed below.

Equation (1) contains several quantities that are important to define properly in the context of this work. First and foremost, ν is the unperturbed eigenfrequency of the considered g-mode or g-dominated mixed mode. While ν is often directly associated with $\nu_{\rm max}$ in this specific context (e.g., Li et al. 2023; Villate et al. 2026), it originally referred to the eigenfrequency of a specific g-dominated mixed mode. The function K is the asymptotic magnetic kernel sensitivity function (Li et al. 2022),

$$K(r) = \frac{\frac{1}{\rho}\left(\frac{N}{r}\right)^3}{\int_{r_{\rm i}}^{r_{\rm o}}\left(\frac{N}{r}\right)^3\frac{{\rm d}r}{\rho}}, \tag{2}$$

which quantifies the sensitivity of the oscillation mode to the magnetic field at the radius coordinate r, with N and ρ being the Brunt-Väisälä frequency and the density of the stellar medium, respectively. The quantity $\overline{B_r}$ in Eq. (1) represents the horizontally averaged, radial magnetic field strength (Li et al. 2022):

$$\overline{B_r}(r)^2 = \frac{1}{4\pi}\iint B_r(r,\theta,\varphi)^2\sin\theta\,{\rm d}\theta\,{\rm d}\varphi\,. \tag{3}$$

Finally, the global magnetic sensitivity, $\mathcal{I}$, referred to as the core structure factor in previous studies, is defined as (Li et al. 2022)

$$\mathcal{I} = \frac{\int_{r_{\rm i}}^{r_{\rm o}}\left(\frac{N}{r}\right)^3\frac{{\rm d}r}{\rho}}{\int_{r_{\rm i}}^{r_{\rm o}}\left(\frac{N}{r}\right){\rm d}r}, \tag{4}$$

where ρ is the density of the stellar medium at the radius coordinate r. The parameter $\mathcal{I}$ can be interpreted as the overall sensitivity of the oscillation modes to the magnetic field and can thus be seen as the global counterpart of K. Throughout this paper, we refer to $\mathcal{I}$ as the global magnetic sensitivity.

The integral in Eq. (1) defines an average of the radial magnetic field strength weighted by the magnetic kernel sensitivity function (Li et al. 2022),

$$\langle B_r^2\rangle = \int_{r_{\rm i}}^{r_{\rm o}} K(r)\overline{B_r}(r)^2\,{\rm d}r, \tag{5}$$

which allows for the definition of the following expression,

$$\langle B_r^2\rangle = \frac{(2\pi)^4\,\mu_0\delta\nu_{\rm mag}\nu^3}{\mathcal{I}}. \tag{6}$$

Equation (6) provides an estimate of the weighted average of the radial magnetic field strength without requiring the assumption of a specific field geometry. In practice, the parameters $\delta\nu_{\rm mag}$ and ν are obtained from asteroseismic measurements, while the global magnetic sensitivity, $\mathcal{I}$, must be inferred using stellar models. The construction of a representative model is thus crucial to properly constrain $\mathcal{I}$ and hence $\langle B_r^2\rangle$. Throughout the rest of this paper, we use the notation $B_{\rm avg} = \sqrt{\langle B_r^2\rangle}$ to refer to the weighted average of the radial magnetic field strength.

As single-star and mass-gain stars of identical mass can possess different internal structures (Rui & Fuller 2021), we expect to find different values for $\mathcal{I}$. As a result, we further expect different values for $B_{\rm avg}$ for the two assumed evolutionary histories. In a similar manner, we expect that the asymptotic magnetic sensitivity kernel, K, may differ between a mass-gain and single-star evolutionary histories at identical total masses.

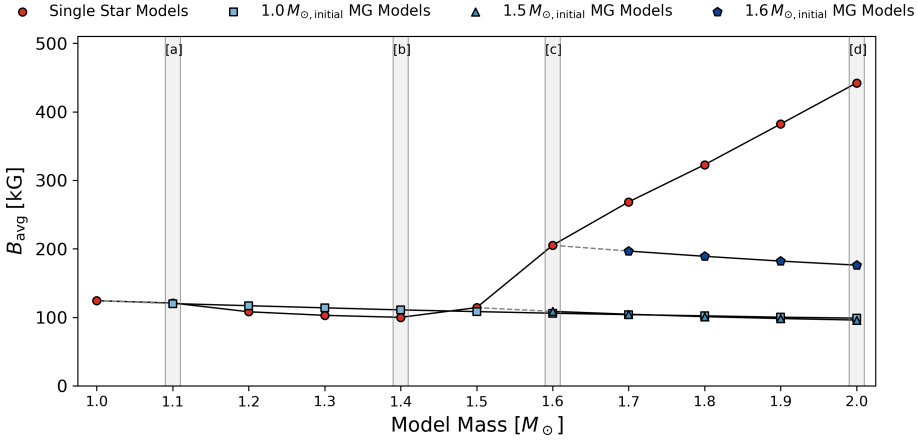


Fig. 1. Weighted average of the radial magnetic field strength, B_{avg}, needed to produce a mean magnetic shift, $\delta\nu_{\mathrm{mag}}$, of 0.2 μHz at a frequency of $\nu_{\mathrm{max}} = 180$ μHz for the single-star and mass-gain models. Here, the values for B_{avg} computed for the single-star models are shown by red dots, and the values for the mass-gain models are shown by light blue squares ($M_{\mathrm{init}} = 1.0\,M_\odot$), blue triangles ($M_{\mathrm{init}} = 1.5\,M_\odot$), and dark blue pentagons ($M_{\mathrm{init}} = 1.6\,M_\odot$). The dashed gray lines connect the values of B_{avg} computed for the mass-gain models to the value of B_{avg} computed for the single-star model corresponding to their respective initial mass, while the gray areas mark the representative models (see Table 1).

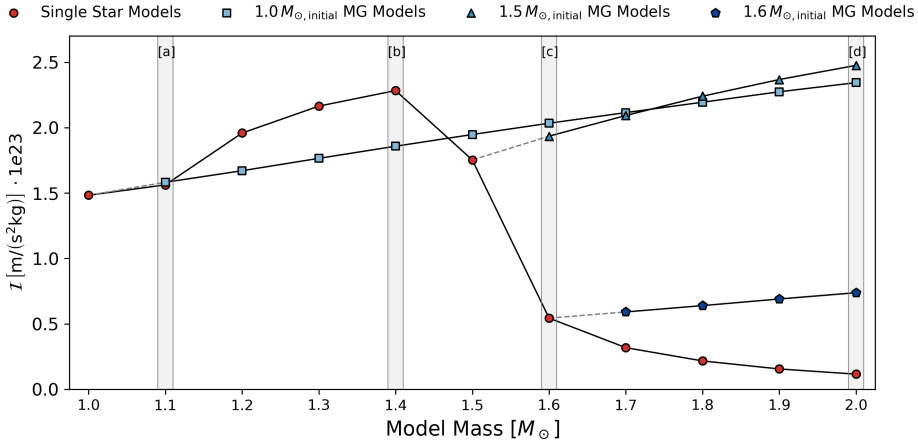


Fig. 2. Global magnetic sensitivity, $\mathcal{I}$, obtained for mass-gain and single-star models at a frequency value for the global power excess of $\nu_{\mathrm{max}} = 180$ μHz. The $\mathcal{I}$ values obtained for the single-star models are shown by red dots and the values for the mass-gain models are shown by light blue squares ($M_{\mathrm{init}} = 1.0\,M_\odot$), blue triangles ($M_{\mathrm{init}} = 1.5\,M_\odot$), and dark blue pentagons ($M_{\mathrm{init}} = 1.6\,M_\odot$). The dashed gray lines connect the $\mathcal{I}$ values obtained for the mass-gain models to that of the single-star model corresponding to their respective initial masses, while the gray areas mark the $\mathcal{I}$ values obtained for the representative models listed in Table 1.

3.2. Impact of mass gain on magnetic frequency shifts

We compared the values of B_{avg} obtained from the single-star and mass-gain models to study how a mass-gain event influences the sensitivity of mixed modes to the magnetic field. The following sections present the results of this investigation.

3.2.1. Model and mass dependence of the inferred field strength

For all of the models, we uniformly assumed a mean magnetic frequency shift of $\delta\nu_{\mathrm{mag}} = 0.2$ μHz for an assumed g-dominated dipole mixed mode. We took the frequency of this assumed g-dominated mixed mode as being identical to the model frequency of ν_{max}. The value for $\delta\nu_{\mathrm{mag}}$ that we considered thus represents the frequency shift fitted at ν_{max}. Due to our extraction criterion in ν_{max} stated in Sect. 2, we consider a mode frequency of $\nu = 180$ μHz for all our models. The assumed frequency value for the magnetic shift falls well into the measured frequency range for $\delta\nu_{\mathrm{mag}}$ (e.g., the value reported for KIC 8684542 in Li et al. 2022). By calculating $\mathcal{I}$ from each MESA profile, we then inferred the value of B_{avg} via Eq. (6). This approach can also be interpreted as finding the magnetic field strength necessary to cause the magnetic shift. In this sense, it is possible to establish a clear connection between the value of B_{avg} and the mode sensitivity to the magnetic field, with lower values of B_{avg} corresponding to higher sensitivities and vice versa. We show the resulting values of B_{avg} in Fig. 1.

Since the magnetic frequency shift is fixed at the same value for all models, any difference in B_{avg} is purely due to a model-dependent difference in the global sensitivity parameter, $\mathcal{I}$, which is closely related to the properties of the model radiative core (see Eq. (4)). For the single-star models (red points), Fig. 1 shows a clear two-regime behavior in terms of mass, with the transition occurring between 1.5 and 1.6 $M_\odot$. We found that the transition mass is sensitive to ν_{max} and shifts towards lower masses for larger ν_{max} values and to larger masses for lower ν_{max} values. Single-star models with masses below the transition mass produce the same frequency shift at lower B_{avg}, which is consistent with the findings of Buchele et al. (2026), indicating a higher sensitivity to the magnetic field compared to their counterparts with masses above the transition mass.

For our mass-gain models (blue symbols in Fig. 1), no such transition is present. Instead, B_{avg} shows a slight decrease with increasing total model mass for models with $M_{\mathrm{init}} = 1.0\,M_\odot$ and $M = 1.5\,M_\odot$. Models with $M_{\mathrm{init}} = 1.6\,M_\odot$ are an exception, showing a higher B_{avg} and thus lower sensitivity to the magnetic field than mass-gain models with initial masses of $M_{\mathrm{init}} = 1.0\,M_\odot$ and $1.5\,M_\odot$. Above a total mass of $\approx 1.5\,M_\odot$, all mass-gain models show a lower B_{avg} and thus higher sensitivity to the field than the single-star models of corresponding mass.

3.2.2. Dependency on stellar core structure and the global magnetic sensitivity

The behavior seen in Fig. 1 can be explained by the differences in the global magnetic sensitivity of mass-gain and single-star models depicted in Fig. 2, which itself arises due to differences in the structure of the model cores. As the effect exerted by

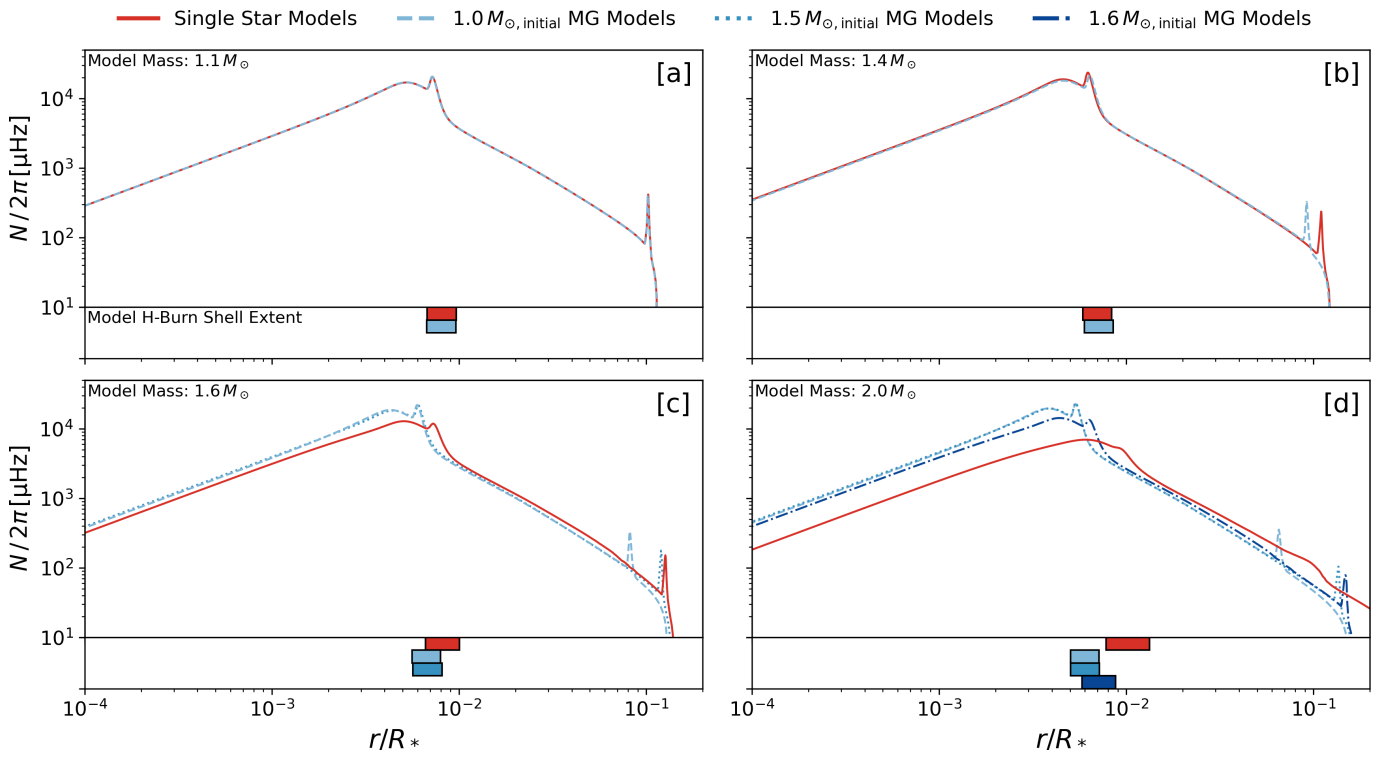


Fig. 3. Brunt-Väisälä frequency as well as the model-specific extent of the hydrogen-burning shell obtained for the representative single-star and mass-gain models at a value for the frequency of the global power excess of $\nu_{\max} = 180\,\mu$Hz. The colored boxes at the bottom of each panel signify the extent of the hydrogen-burning shell of the respective single-star or mass-gain model. The labels [*a*], [*b*], [*c*], and [*d*] correspond to the model labeling introduced in Table 1.

a mass-gain event on the structure of the radiative model core is negligible (Rui & Fuller 2021), mass-gain models possess a core that is very similar to that of an RGB single-star model whose mass is identical to their initial mass. The global magnetic sensitivity is mainly determined by the Brunt-Väisälä profile model (see Eq. (4)), which is conserved during the mass-gain event; this is visible in Fig. 3. Another parameter capable of influencing the value of the global magnetic sensitivity is the model density ρ, as is evident from Eq. (4). We find that the model density, ρ, is roughly conserved during the mass-gain event. This causes a significant difference in the ρ profiles of mass gain and single stars at identical total masses of $M_{\mathrm{total}} > 1.5\,M_\odot$; this is visible in Fig. A.3. As a result, mass-gain models will show a similar value for $\mathcal{I}$, and thus B_{avg}, before and after the mass-gain event, as their N and ρ profiles barely change.

Figure 2 shows the increase in $\mathcal{I}$ with total mass, M_{total}, for mass-gain models of identical initial mass, M_{init}, is a result of our profile extraction criterion in $\nu_{\max}$. During the assumed mass-gain event, the effective temperature, radius, and mass of the model are altered, which leads to an overall increase of $\nu_{\max}$. The mass-gain event thus has a significant impact on the conditions in the model envelope. Mass-gain models that gain a lot of mass thus take longer to reach the extraction threshold of $\nu_{\max} = 180\,\mu$Hz compared to models that gain less mass, allowing the cores of the latter to evolve for a longer time. This results in models that gain more mass possessing more evolved cores, causing the constant increase of $\mathcal{I}$ with mass, as visible in Fig. 2. This behavior is illustrated in Fig. A.2, in which we show the relationship between $\nu_{\max}$ and $\mathcal{I}$ under the consideration of a mass-gain event. For clarity, we show only mass-gain models with $M_{\mathrm{init}} = 1.0\,M_\odot$ in Fig. A.2. However, the behavior is consistent for all mass-gain models. As all mass-gain models of identical M_{init} possess cores that mainly differ in their degree of evolution, it follows that the trend of $\mathcal{I}$ and B_{avg} with mass can be extended to also incorporate the single-star model of mass M_{init}, as is indicated by the dashed lines in Fig. 1 and Fig. 2.

In addition to $\mathcal{I}$, the behavior of the asymptotic sensitivity-kernel function, K, is of interest as it represents the local sensitivity of oscillation modes to the magnetic field. In Fig. A.4, we present the K profiles as well as their cumulative profiles for the representative single-star and mass-gain models. The correlation of the peak of K and the Brunt-Väisälä frequency (e.g., Li et al. 2022) emerges directly from the $K \propto N^3$ dependence visible in Eq. (2). In the literature, it is common to treat B_{avg} as an estimate of the magnetic field strength near the hydrogen-burning shell, owing to the sensitivity of K to the Brunt-Väisälä frequency (e.g., Li et al. 2022). From Fig. A.4, we find that this assumption is even more accurate for mass-gain models, as the cumulative profiles for K show the largest increase in a very narrow region in terms of radius around the hydrogen-burning shell at all total masses considered in the figure.

In summary, the model- and mass-dependent differences of B_{avg}, $\mathcal{I}$, and K that emerge for constant $\delta\nu_{\mathrm{mag}}$ and ν can be directly traced back to differences in the N and ρ profiles of the two model types at identical total masses that arise due to the mass-gain event. In particular, the mass-gain event changes the relationship between the properties of the model core and model envelope. Thus, any fitting method that assumes standard single-star evolution risks yielding an incorrect value for the global magnetic sensitivity and, consequently, a biased estimate of B_{avg} when performed for a mass-gain remnant.

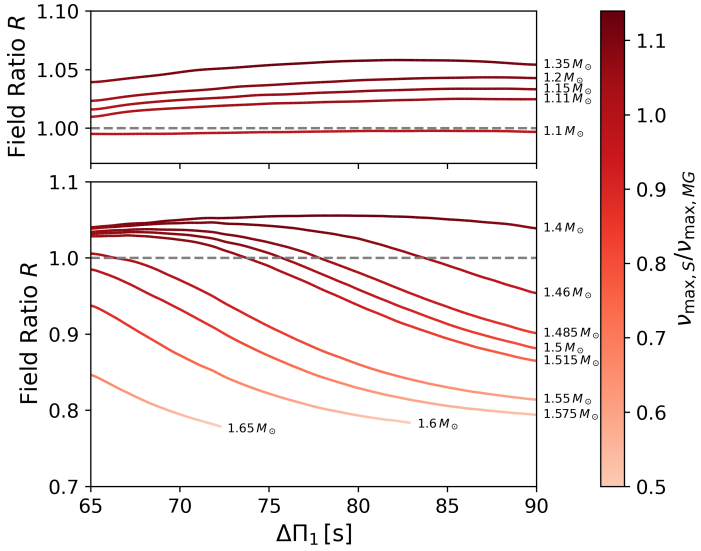


Fig. 4. Ratio, R_B, of the weighted average of the radial magnetic field strength, B_{avg}, of the mass-gain and single-star models needed to produce a magnetic shift of 0.2 μHz for a parameter space spanned by the asymptotic period spacing of dipole g-modes, $\Delta\Pi_1 \in [65\,s, 90\,s]$, and total model mass, $M \in [1.1\,M_\odot, 2.0\,M_\odot]$. The different tracks for R_B are color-coded according to the ν_{max} ratio of the compared models. Dashed lines indicate $\Delta\Pi_1 - R_B$, for which the model difference in ν_{max} is greater than 50%. The top panel shows the R_B tracks for a mass regime of $M \in [1.1\,M_\odot, 1.35\,M_\odot]$ and the bottom panel shows the R_B tracks for a mass regime of $M \in [1.4\,M_\odot, 2.0\,M_\odot]$.

3.2.3. Evolutionary change of the magnetic field strength ratio, R

In order to compare mass-gain and single-star models throughout different evolutionary stages, we define the magnetic field strength ratio as

$$R_B = \frac{B_{MG}}{B_S} = \sqrt{\frac{\mathcal{I}_S}{\mathcal{I}_{MG}}}, \tag{7}$$

where B_S and B_{MG} are the field strengths calculated for single-star and mass-gain models of identical total model mass. The definition of R_B allowed us to visualize the relative evolution of B_{avg} for single-star and mass-gain models along a chosen evolutionary parameter.

Up to this point, we have used ν_{max} to determine the point in stellar evolution at which we performed our seismic analysis on the models. Our choice was motivated by the requirement of having the frequency ν of the g-dominated mixed mode as close to ν_{max} as possible. This ensures that the mixed-mode and thus the magnetic frequency shift is indeed measurable at the considered frequency. However, while this partially constrains the stellar envelope conditions across single-star and mass-gain models, the core parameters are left virtually unconstrained. We now add an extraction parameter that is better suited to constraining the stellar core (Deheuvels et al. 2022; Villate et al. 2026), the asymptotic period spacing of dipole g-modes (e.g., Aerts et al. 2010):

$$\Delta\Pi_1 = \frac{2\pi^2}{\sqrt{2}} \left(\int_{r_i}^{r_o} \frac{N}{r}\, dr \right)^{-1}. \tag{8}$$

We now compare models at multiple values of $\Delta\Pi_1$ in order to understand the evolutionary behavior of R_B at different model masses. We chose to study R_B for the mass-gain models with initial masses of $M_{init} = 1.0\,M_\odot$ in a parameter space spanned by $\Delta\Pi_1 \in [65\,s, 90\,s]$ and $M \in [1.1\,M_\odot, 2.0\,M_\odot]$. The resulting evolution of R_B along $\Delta\Pi_1$ is shown in Fig. 4.

Due to our change of the extraction parameter to $\Delta\Pi_1$, the values for ν_{max} differ significantly between the compared models. This mismatch is problematic, as we still impose that $\delta\nu_{mag}$ and ν are identical when calculating R_B. If the values for ν_{max} of the compared single-star and mass-gain models are too far apart, the observation of a mixed mode and, as a result, the measurement of $\delta\nu_{mag}$ would not be feasible at identical ν in both models. To address this, we imposed an observability condition on ν_{max} by defining the ratio $R_{\nu_{max}} = \frac{\nu_{max,S}}{\nu_{max,MG}}$. When $R_{\nu_{max}} \in [0.5,\ 1.5]$, we considered mixed modes of identical frequency to be observable; this is indicated by the solid lines in Fig. 4. Outside this range, we treat them as unobservable simultaneously, and they are, as a result, not included in Fig. 4.

From Fig. 4, we find that different total model masses result in distinct trends of the $\Delta\Pi_1 - R_B$ curve. We find that R_B ranges from 1 to 1.05 when the total model mass is below $1.4\,M_\odot$ with little dependence on $\Delta\Pi_1$ (see the upper panel of Fig. 4). The mass range $1.4\,M_\odot < M < 1.6\,M_\odot$ marks a transition region in which R_B changes with $\Delta\Pi_1$, showing an increase with decreasing $\Delta\Pi_1$. The difference in the R_B tracks is a direct result of the structural differences of the model core owing to the assumed mass-gain event (see Sect. 3.2.2).

In summary, we find that the difference in B_{avg} inferred for mass-gain and single-star models at identical values for $\Delta\Pi_1$ is up to 25% in the considered $\Delta\Pi_1 - M$ parameter space when considering modes that are observable in both single-star and mass-gain models. We furthermore find that in the considered $\Delta\Pi_1$ range, all models with total masses of $>1.65\,M_\odot$ cannot fulfill our observability criterion.

3.3. B_{avg} estimates for possible magnetic merger remnants

Having established the impact of a mass-gain event on the sensitivity of stellar oscillations to the magnetic field, we then applied these findings to two RGB stars that have been identified as possible merger candidates in the literature. The recent work of Villate et al. (2026) reports the magnetic field strength for several seismically active RG stars, including KIC 4350501, which was already identified as a merger candidate by Deheuvels et al. (2022) because its $\Delta\nu$ and $\Delta\Pi_1$ values place it well below the degeneracy sequence (see Deheuvels et al. 2022) in the $\Delta\nu$-$\Delta\Pi_1$ diagram. From the magnetic RG sample of Hatt et al. (2024), we identified KIC 9508757, which also exhibits a $\Delta\nu/\Delta\Pi_1$ combination inconsistent with standard single-star evolution. In this section, we demonstrate that it is possible to construct acceptable models for both KIC 4350501 and KIC 9508757 and to constrain measures for the magnetic field strength under the assumption of a mass-gain history.

3.3.1. Definition of the stellar model grid

As our original model grid assumes a constant metallicity for all models and the resolution of the initial- and post-gain mass parameters is insufficient, we computed a new mass-gain model grid consisting of 1320 model tracks. The mass and metallicity ranges were chosen to encompass the literature values for mass (Yu et al. 2018) and metallicity (Mathur et al. 2017) for KIC 4350501 and KIC 9508757. We varied the models in initial mass ($M_{init} \in [1.2\,M_\odot, 1.45\,M_\odot]$, $\Delta M_{init} = 0.05\,M_\odot$), post-gain

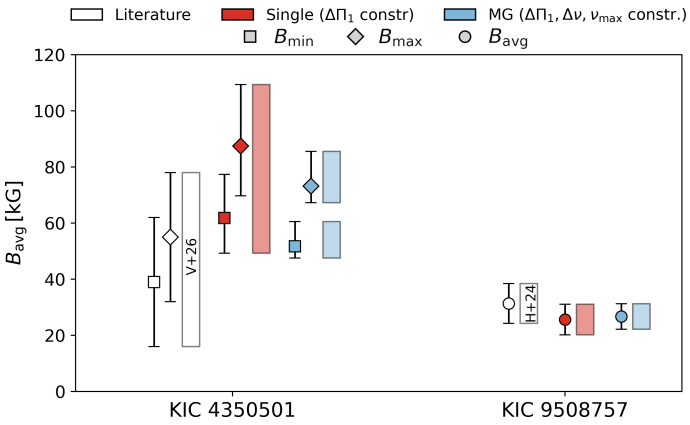


Fig. 5. Comparison of the values for B_{avg} (circles) for KIC 9508757 and B_{min} (squares) and B_{max} (diamonds) for KIC 4350501 yielded from our mass-gain and single-star model grid and the corresponding literature values reported in Hatt et al. (2024) (Indicated by the H+24 label) and Villate et al. (2026) (Indicated by the V+26 label), respectively. The values obtained for the best-fitting models are indicated by markers, while the total uncertainty range is indicated by colored rectangles.

mass ($M \in [1.5\,M_\odot, 2.0\,M_\odot]$, $\Delta M = 0.05\,M_\odot$), initial metallicity ([Fe/H] $\in [-0.36\,\mathrm{dex}, -0.08\,\mathrm{dex}]$, Δ[Fe/H] = 0.07 dex), and the mixing length parameter ($\alpha_{MLT} \in [2.0, 2.6]$, $\Delta\alpha_{MLT} = 0.2$). To test whether we could find a fitting model assuming a conventional single-star evolution, we computed an additional grid consisting of 300 single-star models. The models vary in initial mass ($M_{init} \in [1.3\,M_\odot, 2.0\,M_\odot]$, $\Delta M_{init} = 0.05\,M_\odot$), metallicity, and the mixing length parameter, with grid points identical to those of the mass-gain model grid.

3.3.2. Fitting of the model grids

We identified the best-fitting model by calculating χ^2_{fit} following the same approach as Villate et al. (2026),

$$\chi^2_{fit} = \frac{(\Delta\nu_o - \Delta\nu_m)^2}{\sigma^2_{\Delta\nu}} + \frac{(\Delta\Pi_{1,o} - \Delta\Pi_{1,m})^2}{\sigma^2_{\Delta\Pi_1}} + \frac{(\nu_{max,o} - \nu_{max,m})^2}{\sigma^2_{\nu_{max}}}, \quad (9)$$

where the subscript m refers to model values and the subscript o to observational values taken from Hatt et al. (2024), and Villate et al. (2026) ($\Delta\Pi_1$ and $\Delta\nu$) and Yu et al. (2018) (ν_{max}), with σ_i being the corresponding stated uncertainties. We adopted this definition as the parameters $\Delta\nu$, ν_{max}, and $\Delta\Pi_1$ jointly constrain both the core and envelope parameters of the model. Constraining only the envelope or the core leads to large uncertainties in $\mathcal{I}$, as shown in Sect. 3.2.2 and Sect. 3.2.3. We expect that constraining both regions simultaneously reduces these uncertainties.

We calculated $\Delta\nu$ using the radial modes found by the GYRE stellar oscillation code (Townsend & Teitler 2013) in the five radial orders closest to ν_{max}. We define $\Delta\nu$ to be the slope of a linear fit of the corresponding $\ell = 0$ mode frequencies (for the methodology; e.g., Grossmann et al. 2025). To mitigate the effects of coarse evolutionary resolution, we linearly interpolated $\Delta\Pi_1$, ν_{max}, and $\Delta\nu$ onto a grid 1000 times finer in terms of model age.

In the case of KIC 4350501, we find three mass-gain models for which $\chi^2_{fit} < 2$. In order to find a fitting model for KIC 9508757, we loosened the acceptance threshold to $\chi^2_{fit} < 6$, which is fulfilled by four mass-gain models. Although only a small number of mass-gain models satisfy our fitting criteria, we consider it sufficient for our proof-of-concept approach, as a detailed fitting of these targets is beyond the intended scope of this work.

For the single-star model grid, we were, as in the literature, not able to find an acceptable model. The best-fitting single-star models show $\chi^2_{fit} \approx 10^3$–$10^4$ in the case of both KIC 4350501 and KIC 9508757. For comparison purposes, we employed the following loosened fitting prescription used by Villate et al. (2026), which solely constrains $\Delta\Pi_1$, for our single-star model grid:

$$\chi^2_{fit,s} = \frac{(\Delta\Pi_{1,o} - \Delta\Pi_{1,m})^2}{\sigma^2_{\Delta\Pi_1}}. \quad (10)$$

We slightly tightened the new fitting criterion by additionally demanding that fitting models must fulfill the observability condition in ν_{max} defined in Sect. 3.2.3, rejecting all models that show a $\nu_{max,m}$ deviating from $\nu_{max,o}$ by more than 50%. This constrains the core properties but only very loosely constrains the envelope properties for the single-star models. We thus expect the model uncertainties discussed in Sect. 3.2.3 to emerge. Applying the fitting criterion defined in Eq. (10), we were able to find an abundance of single-star models fulfilling $\chi^2_{fit} < 2$.

3.3.3. Magnetic field estimates

By calculating $\mathcal{I}$ from the fitting single-star and mass-gain models and assuming the values for $\delta\nu_{mag}$ reported in Hatt et al. (2024) and Villate et al. (2026), we estimated B_{avg} following Eq. (6) for KIC 9508757. However, due to the doublet nature of the $\ell = 1$ mixed modes of KIC 4350501, Villate et al. (2026) could not constrain the asymmetry parameter, a. As a result, they obtained an interval of possible field strengths bounded by B_{min} and B_{max}, which are defined as (Villate et al. 2026)

$$B_{min} = \left(\frac{2}{3}\frac{(2\pi)^4\,\mu_0\delta\nu_{mag}\nu^3}{\mathcal{I}}\right)^{1/2}, \quad B_{max} = \left(\frac{4}{3}\frac{(2\pi)^4\,\mu_0\delta\nu_{mag}\nu^3}{\mathcal{I}}\right)^{1/2}, \quad (11)$$

which we also adopted in the case of KIC 4350501.

We estimated the uncertainty in B_{avg}, B_{min}, and B_{max} from the reported uncertainties in $\delta\nu_{mag}$ and ν_{max}. For $\mathcal{I}$, we adopted a model uncertainty equal to half the range spanned by the values obtained from the fitting models. For comparison, the uncertainty implied by our single-star model grid corresponds to 27% of the mean value of $\mathcal{I}$ across all fittings single-star models and is in good agreement with the value uncertainty reported by Hatt et al. (2024). We compared our values to the previously reported measurements.

3.3.4. Discussion and comparison with literature

The inferred values for B_{min}, B_{max}, and B_{avg} calculated for the best-fitting single-star and mass-gain models compared to the values found by Hatt et al. (2024) and Villate et al. (2026) are shown in Fig. 5. While the B_{avg} estimate for KIC 9508757 is broadly consistent with that of Hatt et al. (2024), we find a significant offset relative to the value reported by Villate et al. (2026) for KIC 4350501. As this offset in B_{min} and B_{max} appears for both the single-star and mass-gain results, we attribute it to differences in the stellar model prescriptions used by us and those used by Villate et al. (2026), an effect first discussed in Buchele et al. (2026).

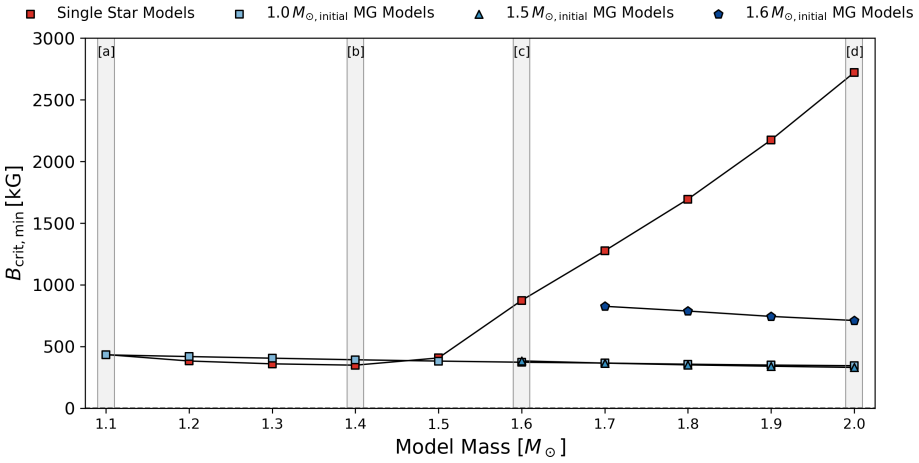


Fig. 6. Minimum critical magnetic field strength, $B_{\mathrm{crit,min}}$, required to suppress the mixed dipole modes in the mass-gain and single-star models at a frequency of $\nu = \nu_{\max} = 180\,\mu$Hz. The values for $B_{\mathrm{crit,min}}$ yielded for the single-star models are marked by red dots, while the values for $B_{\mathrm{crit,min}}$ for the mass-gain models are signified by light blue squares ($M_{\mathrm{init}} = 1.0\,M_\odot$), blue triangles ($M_{\mathrm{init}} = 1.5\,M_\odot$), and dark blue pentagons ($M_{\mathrm{init}} = 1.6\,M_\odot$). The gray areas mark the yielded values for the representative models (see Table 1).

The ranges of $B_{\min}$ and $B_{\max}$ spanned by the fitting mass-gain models in the case of KIC 4350501 are significantly smaller than those obtained from the fitting single-star models. While the difference in B_{avg} is less pronounced in the case of KIC 9508757, the range spanned by the fitting mass-gain models is still smaller compared to the range spanned by the fitting single-star models. As the envelope is nearly unconstrained for the fitting single-star models, the effects discussed in Sect. 3.2.3 cause a spread in $B_{\min}$, $B_{\max}$, and B_{avg}. In contrast, fitting both $\Delta\nu$ and $\nu_{\max}$ in addition to $\Delta\Pi_1$ in the mass-gain models also tightly constrains the model envelope and therefore reduces model ambiguity.

The model parameters we obtained for $\Delta\Pi_1, \Delta\nu$, mass, radius, and metallicity in the case of the fitting mass-gain models agree well with the values reported in literature (Mathur et al. 2017; Yu et al. 2018; Hatt et al. 2024; Villate et al. 2026); however, we find that the effective temperature, T_{eff}, of the model stars is significantly higher than the observational values reported in Yu et al. (2018), especially in the case of KIC 4350501 (5σ difference between $T_{\mathrm{eff,o}}$ and $T_{\mathrm{eff,m}}$ for KIC 4350501 and 2σ difference for KIC 9508757). We also find that $\nu_{\max}$ lies within 3σ of the observational values reported by Yu et al. (2018) in the case of KIC 9508757, which explains the necessity of relaxing the χ^2 fitting threshold to a value of six. We attribute this offset to the toy-model mass-gain approach we used and recommend that mass accretion be carefully simulated when measuring magnetic field strength on potential merger products. Due to the discrepancy in T_{eff} and $\nu_{\max}$, we emphasize that the parameter intervals for $B_{\min}$, $B_{\max}$, and B_{avg} calculated by us are not necessarily more accurate than the values reported in Villate et al. (2026) and Hatt et al. (2024). We do, however, argue that for a self-consistent model prescription, the assumption of a mass-gain scenario allows $B_{\min}$, $B_{\max}$, and B_{avg} to be more tightly constrained as it allows for the simultaneous constraining of the model envelope and model core.

In summary, for a weak magnetic field the oscillations of mass-gain models with initial masses $\leq 1.6\,M_\odot$ show a greater sensitivity to the magnetic field than those of single-star models above a total mass threshold of $\gtrsim 1.5\,M_\odot$ when the mass-gain event is simulated during the early RGB evolutionary phase and the models are evaluated at $\nu_{\max} = 180\,\mu$Hz (see Fig. 2). This exact value of the threshold depends on $\nu_{\max}$, but the qualitative behavior remains the same. We recovered an analog behavior when comparing mass-gain and single-star models at identical values of $\Delta\Pi_1$ (see Fig. 4). This difference in sensitivity is a direct consequence of the conservation of the N profile during the mass-gain event (see Fig. 3), which determines the global magnetic sensitivity parameter, $\mathcal{I}$ (see Eq. (4)). As a result, mass-gain models above the mass threshold show stronger magnetic signatures in their oscillations than single-star models at identical values for B_{avg}. When estimating B_{avg} for a mass-gain candidate, adopting a mass-gain evolutionary history provides a tighter constraint of both the global magnetic sensitivity and B_{avg}, as it allows for the simultaneous constraining of the core and envelope properties.

4. Influence of strong magnetic fields

Moving away from the weak-field limit, we now investigate the impact of strong magnetic fields on stellar oscillations under the assumption of a mass-gain history. Specifically, we assumed core fields that reach or exceed the critical magnetic field strength, B_{crit}, the threshold above which the gravity-wave component of dipole mixed modes becomes converted into magnetic waves (e.g., Fuller et al. 2015; Stello et al. 2016a,b; Lecoanet et al. 2017; Loi & Papaloizou 2020; Müller et al. 2025).

4.1. Mode suppression due to magnetism

To explain the observed population of RG stars with suppressed mixed dipole modes (e.g., García et al. 2014; Stello et al. 2016b), the study of Fuller et al. (2015) showed that magnetic fields can suppress mixed dipole modes if the magnetic field strength somewhere in the stellar interior exceeds a critical value of

$$B_{\mathrm{crit}} = \sqrt{\frac{\pi\rho}{2}}\frac{(2\pi)^2\,\nu^2 r}{N}, \tag{12}$$

with Lecoanet et al. (2017) further showing that this suppression happens due to the gravity wave component being converted into magnetic waves. In the case of RGs, the minimum critical field strength necessary to cause such a conversion,

$$B_{\mathrm{crit,min}} = \min\left(B_{\mathrm{crit}}\,(r)\right), \tag{13}$$

is located at the hydrogen-burning shell, where the Brunt-Väisälä frequency reaches its maximum (see Fig. 3), owing to the $B_{\mathrm{crit}} \propto 1/N$ relation found in Eq. (12).

4.2. Dependence of the critical field strength, B_{crit}, on the assumed mass-gain history

As the core structure is largely conserved during a mass-gain event (Rui & Fuller 2021), we expected $B_{\mathrm{crit,min}}$ to differ between

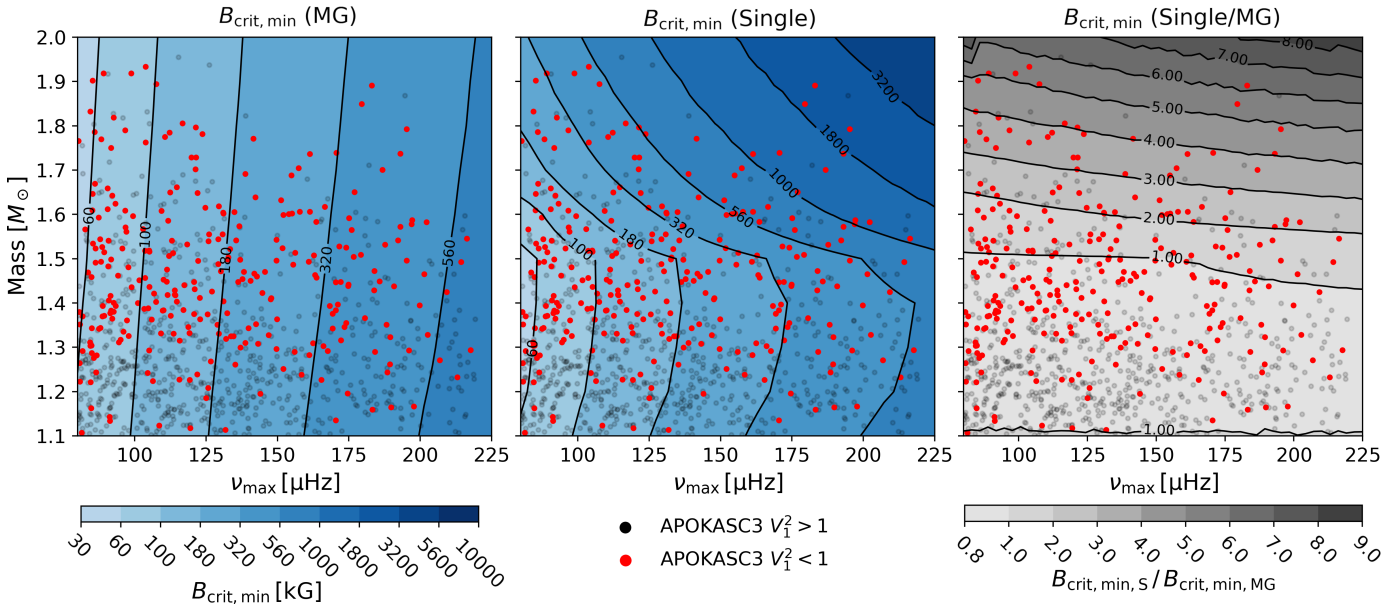


Fig. 7. Parameter space taken on by $B_{\rm crit,min}$ under the assumption of a $M_{\rm init} = 1.0\,M_\odot$ mass-gain evolutionary history (left) and a single-star evolutionary history (middle), as well as the ratio of $B_{\rm crit,min}$ corresponding to the $M_{\rm init} = 1.0\,M_\odot$ mass-gain or single-star assumption (right). The labeled curves in the background of the plots correspond to the contour lines of $B_{\rm crit,min}$ (left and middle panels) and the $B_{\rm crit,min}$ ratio between mass gain and single stat models (right panel) at different mass and $\nu_{\rm max}$ combinations. Targets that are listed in the APOKASC3 catalog as possessing low dipole mode visibilities are indicated by red dots, while targets that show normal dipole mode visibilities are indicated by transparent black dots.

the single-star and mass-gain models. We focused in particular on higher model masses, where the global magnetic sensitivity between the two evolutionary scenarios diverges most strongly (see Sect 3.2.1 and Sect. 3.2.2). Figure 6, in which we assume $\nu = \nu_{\rm max}$ for all depicted models, confirms this expected behavior of $B_{\rm crit,min}$. While the single-star models exhibit the expected steep increase in $B_{\rm crit,min}$ for model masses above 1.5 $M_\odot$ (see Fuller et al. 2015; Stello et al. 2016b), $B_{\rm crit,min}$ barely changes with model mass for the mass-gain models, owing to their similar core structure.

Notably, $B_{\rm crit,min}$ remains in the range of a few hundred kilogauss for all mass-gain models with $M_{\rm init} < 1.5\,M_\odot$, which is substantially below the >1 MG values obtained for the corresponding high-mass single-star models. As shown by Stello et al. (2016b), a significant fraction of *Kepler* RG stars with masses of $>1.6\,M_\odot$ (about 60% in their sample) show depressed mixed dipole modes. To explain the observed mode suppression in these targets using the model of Fuller et al. (2015), very strong magnetic fields on the order of several hundred kilogauss up to multiple megagauss would be required. Using the dipole mode visibility, V_1^2, reported in the APOKASC3 catalog (Stello et al. 2016b; Pinsonneault et al. 2025) and the single-star and mass-gain models, we recreated Fig. 2 of Stello et al. (2016b) in the middle panel of Fig. 7; in the former, the authors showed the parameter space occupied by $B_{\rm crit\,min}$ for different values for M and $\nu_{\rm max}$. We expanded this analysis by calculating the parameter space of $B_{\rm crit,min}$ under the assumption of a mass-gain evolutionary history. For the mass-gain models, we assumed a common initial mass of $M_{\rm init} = 1.0\,M_\odot$. The resulting parameter space of $B_{\rm crit,min}$ for the mass-gain and single-star evolutionary history is presented in the left and right panels of Fig. 7, respectively. We also show the ratio of $B_{\rm crit,min}$ between the single-star and mass-gain histories in the right panel of Fig. 7. We find that adopting a $M_{\rm init} = 1.0\,M_\odot$ mass-gain history reduces the critical field strength required to explain depressed dipole modes in RG stars with $M > 1.6\,M_\odot$ and $\nu_{\rm max} \gtrsim 170\,\mu$Hz from $B_{\rm crit,min} \gtrsim 1$ MG to $B_{\rm crit,min} \lesssim 600$ kG. Albeit still a considerably high value, this lies within the range of reported values for the weighted average of the radial field strength of RGB stars (see Deheuvels et al. 2023). While not all depressed stars with masses exceeding 1.6 $M_\odot$ can necessarily be identified as mass-gain products, the fact that mass-gain evolutionary scenarios require substantially weaker magnetic fields to show suppression of mixed dipole modes suggests a promising explanation that warrants further exploration in future studies.

5. Conclusion

In this work, we quantified the degeneracy introduced to the local and global sensitivity of stellar oscillation modes and to an internal magnetic field when different stellar evolutionary histories are considered for low- to intermediate-mass, RGB solar-like oscillators. In our study, we compared stellar models that experienced a mass-gain event during the early RGB phase to stellar models showing a typical single-star evolution in a mass range of 1.1 $M_\odot$ to 2 $M_\odot$. We performed our analysis in two regimes: the weak-field regime, where fields induce a magnetic frequency shift to mixed dipole modes, and the strong-field regime, where fields are strong enough to suppress mixed dipole modes. Our results demonstrate that the assumed stellar evolutionary history has a strong impact when inferring the parameters of internal magnetic fields through asteroseismology.

In the weak-field regime, we demonstrate that for a g-dominated mode with a given frequency of ν and magnetic frequency shift of $\delta\nu_{\rm mag}$, the inferred value of the weighted average of the radial magnetic field strength $\langle B_r^2\rangle^{1/2}$ obtained using the formulation for asymptotic gravity modes (Bugnet et al. 2021; Li et al. 2022) strongly depends on the assumed evolutionary history for models of identical total mass. This effect originates from differences in the global magnetic sensitivity, $\mathcal{I}$, which is closely linked to the Brunt-Väisälä frequency, N, and the model

density, ρ (see Eq. (4)). These differences in $\mathcal{I}$ arise from the conservation of the core structure and thus the N and ρ profile of mass-gain models during the mass-gain event (Rui & Fuller 2021; Deheuvels et al. 2022). We also find that the profile of the asymptotic magnetic sensitivity kernel, K, is conserved during a mass-gain event, owing to its dependence on N and ρ (see Eq. (2)).

We constrained the stellar core properties by evaluating $B_{\rm avg}$ for mass-gain models with an initial mass of $1.0\,M_\odot$ and single-star models of corresponding total mass in the $1.1\,M_\odot$ to $2.0\,M_\odot$ range and calculated the magnetic field ratio, $R_{\rm B}$. We show that for identical $\Delta\Pi_1$, the field strength, $\langle B_r^2\rangle^{1/2}$, obtained for the mass-gain and single-star models, differs by up to 25% when constraints on the model envelope properties are relaxed.

We constructed single-star and mass-gain model grids to estimate $\langle B_r^2\rangle^{1/2}$ for KIC 4350501 and KIC 9508757, two strong merger candidates identified in the literature (Hatt et al. 2024; Villate et al. 2026). We found acceptable mass-gain models with a fitting $\Delta\Pi_1/\Delta\nu/\nu_{\rm max}$ combination for both targets. For both KIC 4350501 and KIC 9508757, adopting a mass-gain evolutionary scenario reduced the range of possible values for $\langle B_r^2\rangle^{1/2}$ relative to the corresponding models of our single-star grid with fitting values for $\Delta\Pi_1$.

In the strong-field regime, we find that a mass-gain evolutionary history substantially reduces the minimum critical field strength, $B_{\rm crit,min}$, required for dipole mode suppression (up to $\approx$80% in the most extreme case). For stars with $M > 1.6\,M_\odot$ and $\nu_{\rm max} \gtrsim 170\,\mu$Hz, we find that $B_{\rm crit,min}$ decreases to values well below 1 MG, which is significantly lower than the values predicted by single-star models occupying the same region in the $\nu_{\rm max} - M$ parameter space. These results suggest that stars with $M > 1.6\,M_\odot$ and high $\nu_{\rm max}$ values that show depressed dipole mixed modes may represent promising mass-gain candidates. We thus propose that the investigation of the evolutionary history of these stars could prove interesting to properly constrain $B_{\rm crit,min}$.

We conclude that magnetic detections in both the weak- and the strong-field regimes can be systematically biased if the evolutionary history of the star is poorly constrained. We thus suggest the inclusion of stellar models that follow a non-single-star evolution in future studies involving the probing of probable merger/mass-gain candidates that show magnetic signatures in their oscillations.

Acknowledgements. L. Buchele, L. Bugnet, and L. Einramhof gratefully acknowledge support from the European Research Council (ERC) under the Horizon Europe programme (Calcifer; PI Bugnet; Starting Grant agreement N°101165631). While partially funded by the European Union, views and opinions expressed are, however, those of the authors only and do not necessarily reflect those of the European Union or the European Research Council. Neither the European Union nor the granting authority can be held responsible for them. L. Barrault acknowledges the support of the Austrian Academy of Sciences through the Doctoral Fellowship Programme (DOC) of the Austrian Academy of Sciences 27648. P. G. Beck acknowledges support by the Spanish Ministry of Science, Innovation and Universities (MCIN) with the *Ramón y Cajal* fellowship (RYC-2021-033137-I). P. G. Beck acknowledge support from MCIN for the project *PLAtoSOnG* from its grant PID2023-146453NB-I00. P. G. Beck was supported by the International Space Science Institute (ISSI) in Bern with the project 24-629. PGB acknowledges financial support from the Agencia Estatal de Investigación (AEI) through the Severo Ochoa Centre of Excellence accreditation awarded to the Instituto de Astrofísica de Canarias, grant CEX2025-001609-S, funded by MICIU/AEI/10.13039/501100011033.

References

Aerts, C., Christensen-Dalsgaard, J., & Kurtz, D. W. 2010, Asteroseismology (Springer Science & Business Media)
Beck, P. G. 2026, A&A, 707, A298
Beck, P. G., Bedding, T. R., Mosser, B., et al. 2011, Science, 332, 205
Beck, P. G., Montalban, J., Kallinger, T., et al. 2012, Nature, 481, 55
Bedding, T. R., Mosser, B., Huber, D., et al. 2011, Nature, 471, 608
Bhattacharya, S., Das, S. B., Bugnet, L., Panda, S., & Hanasoge, S. M. 2024, ApJ, 970, 42
Borucki, W. J., Koch, D., Basri, G., et al. 2010, Science, 327, 977
Buchele, L. 2025, Res. Notes Am. Astron. Soc., 9, 193
Buchele, L., Bugnet, L., Muntean, N., & Hatt, E. 2026, A&A, 713, A294
Bugnet, L. 2022, A&A, 667, A68
Bugnet, L., Prat, V., Mathis, S., et al. 2021, A&A, 650, A53
Cantiello, M., Fuller, J., & Bildsten, L. 2016, ApJ, 824, 14
Ceillier, T., Tayar, J., Mathur, S., et al. 2017, A&A, 605, A111
Cyburt, R. H., Amthor, A. M., Ferguson, R., et al. 2010, ApJS, 189, 240
Das, S. B., Chakraborty, T., Hanasoge, S., & Tromp, J. 2020, ApJ, 897, 38
Das, S. B., Einramhof, L., & Bugnet, L. 2024, A&A, 690, A217
de Mink, S. E., Sana, H., Langer, N., Izzard, R. G., & Schneider, F. R. N. 2014, ApJ, 782, 7
Deheuvels, S., García, R. A., Chaplin, W. J., et al. 2012, ApJ, 756, 19
Deheuvels, S., Doğan, G., Goupil, M. J., et al. 2014, A&A, 564, A27
Deheuvels, S., Brandão, I., Silva Aguirre, V., et al. 2016, A&A, 589, A93
Deheuvels, S., Ballot, J., Eggenberger, P., et al. 2020, A&A, 641, A117
Deheuvels, S., Ballot, J., Gehan, C., & Mosser, B. 2022, A&A, 659, A106
Deheuvels, S., Li, G., Ballot, J., & Lignières, F. 2023, A&A, 670, L16
Deheuvels, S., Ballot, J., Lignières, F., Li, G., & Villate, M. 2026, A&A, 709, A224
Di Mauro, M. P., Ventura, R., Corsaro, E., & Lustosa De Moura, B. 2018, ApJ, 862, 9
Dvoráková, N., Korcáková, D., Dinnbier, F., & Kroupa, P. 2024, A&A, 689, A234
Eddington, A. S. 1926, The Internal Constitution of the Stars
Ferguson, J. W., Alexander, D. R., Allard, F., et al. 2005, ApJ, 623, 585
Fridlund, M., Baglin, A., Lochard, J., & Conroy, L. 2006, The CoRoT Mission Pre-Launch Status – Stellar Seismology and Planet Finding, 1306
Fuller, G. M., Fowler, W. A., & Newman, M. J. 1985, ApJ, 293, 1
Fuller, J., Cantiello, M., Stello, D., Garcia, R. A., & Bildsten, L. 2015, Science, 350, 423
García, R. A., Pérez Hernández, F., Benomar, O., et al. 2014, A&A, 563, A84
Gomes, P., & Lopes, I. 2020, MNRAS, 496, 620
Goode, P. R., & Thompson, M. J. 1992, ApJ, 395, 307
Gough, D. O., & Thompson, M. J. 1990, MNRAS, 242, 25
Grevesse, N., & Sauval, A. J. 1998, Space Sci. Rev., 85, 161
Grossmann, D. H., Beck, P. G., Mathur, S., et al. 2025, A&A, 696, A42
Hasan, S. S., Zahn, J.-P., & Christensen-Dalsgaard, J. 2005, A&A, 444, L29
Hatt, E. J., Ong, J. M. J., Nielsen, M. B., et al. 2024, MNRAS, 534, 1060
Henneco, J., Schneider, F. R. N., Hekker, S., & Aerts, C. 2024, A&A, 690, A65
Henyey, L., Vardya, M. S., & Bodenheimer, P. 1965, ApJ, 142, 841
Herwig, F. 2000, A&A, 360, 952
Irwin, A. W. 2012, Astrophysics Source Code Library [record ascl:1211.002]
Jermyn, A. S., Schwab, J., Bauer, E., Timmes, F. X., & Potekhin, A. Y. 2021, ApJ, 913, 72
Jermyn, A. S., Bauer, E. B., Schwab, J., et al. 2023, ApJS, 265, 15
Kjeldsen, H., & Bedding, T. R. 1995, A&A, 293, 87
Kochanek, C. S., Adams, S. M., & Belczynski, K. 2014, MNRAS, 443, 1319
Kuszlewicz, J. S., Hon, M., & Huber, D. 2023, ApJ, 954, 152
Langanke, K., & Martínez-Pinedo, G. 2000, Nucl. Phys. A, 673, 481
Lecoanet, D., Vasil, G. M., Fuller, J., Cantiello, M., & Burns, K. J. 2017, MNRAS, 466, 2181
Li, G., Deheuvels, S., Ballot, J., & Lignières, F. 2022, Nature, 610, 43
Li, G., Deheuvels, S., Li, T., Ballot, J., & Lignières, F. 2023, A&A, 680, A26
Loi, S. T. 2021, MNRAS, 504, 3711
Loi, S. T., & Papaloizou, J. C. B. 2020, MNRAS, 491, 708
Mathis, S., & Bugnet, L. 2023, A&A, 676, L9
Mathis, S., Bugnet, L., Prat, V., et al. 2021, A&A, 647, A122
Mathur, S., Huber, D., Batalha, N. M., et al. 2017, ApJS, 229, 30
Mestel, L., Tayler, R. J., & Moss, D. L. 1988, MNRAS, 231, 873
Mosser, B., Barban, C., Montalbán, J., et al. 2011, A&A, 532, A86
Mosser, B., Elsworth, Y., Hekker, S., et al. 2012, A&A, 537, A30
Mosser, B., Vrard, M., Belkacem, K., Deheuvels, S., & Goupil, M. J. 2015, A&A, 584, A50
Mosser, B., Pinçon, C., Belkacem, K., Takata, M., & Vrard, M. 2017, A&A, 600, A1
Mosser, B., Gehan, C., Belkacem, K., et al. 2018, A&A, 618, A109
Müller, J., Coppée, Q., & Hekker, S. 2025, A&A, 696, A134
Oda, T., Hino, M., Muto, K., Takahara, M., & Sato, K. 1994, At. Data Nucl. Data Tables, 56, 231

Patton, R. A., Pinsonneault, M. H., & Thompson, T. A. 2025, ApJ, 987, 212
Paxton, B., Bildsten, L., Dotter, A., et al. 2011, ApJS, 192, 3
Paxton, B., Cantiello, M., Arras, P., et al. 2013, ApJS, 208, 4
Paxton, B., Marchant, P., Schwab, J., et al. 2015, ApJS, 220, 15
Paxton, B., Smolec, R., Schwab, J., et al. 2019, ApJS, 243, 10
Pinsonneault, M. H., Zinn, J. C., Tayar, J., et al. 2025, ApJS, 276, 69
Rashba, T. I., Semikoz, V. B., Turck-Chièze, S., & Valle, J. W. F. 2007, MNRAS, 377, 453
Reimers, D. 1975, in Problems in Stellar Atmospheres and Envelopes, eds. B. Baschek, W. H. Kegel, & G. Traving, 229
Ricker, G. R., Winn, J. N., Vanderspek, R., et al. 2015, J. Astron. Telesc. Instrum. Syst., 1, 014003
Rogers, F. J., & Nayfonov, A. 2002, ApJ, 576, 1064
Rui, N. Z., & Fuller, J. 2021, MNRAS, 508, 1618
Stello, D., Cantiello, M., Fuller, J., Garcia, R. A., & Huber, D. 2016a, PASA, 33, e011
Stello, D., Cantiello, M., Fuller, J., et al. 2016b, Nature, 529, 364
Takahashi, K., & Langer, N. 2021, A&A, 646, A19
Tayar, J., Beck, P. G., Pinsonneault, M. H., García, R. A., & Mathur, S. 2019, ApJ, 887, 203
Thompson, M. J., Toomre, J., Anderson, E. R., et al. 1996, Science, 272, 1300
Timmes, F. X., & Swesty, F. D. 2000, ApJS, 126, 501
Townsend, R. H. D., & Teitler, S. 2013, MNRAS, 435, 3406
Unno, W., Osaki, Y., Ando, H., Saio, H., & Shibahashi, H. 1989, Nonradial Oscillations of Stars
Villate, M., Deheuvels, S., & Ballot, J. 2026, A&A, 707, A366
Vrard, M., Mosser, B., & Samadi, R. 2016, A&A, 588, A87
Wu, T., Guo, Z., & Li, Y. 2026, A&A, 705, A164
Yu, J., Huber, D., Bedding, T. R., et al. 2018, ApJS, 236, 42

Appendix A: Additional model information

A.1. Employed model physics of our MESA setup

In this Appendix, we intend to provide further information about the base setup we have employed in all MESA models used in this work. As already stated in Sect. 2, we base our MESA inlists on the work conducted by Rui & Fuller (2021).

We make use of the standard equation of state combination consisting of the OPAL/SCVH blend (Rogers & Nayfonov 2002), HELM (Timmes & Swesty 2000), FreeEOS (Irwin 2012), and SKYE (Jermyn et al. 2021). For our opacity tables in the high and low temperature regime, we choose the standard solar abundances provided by Grevesse & Sauval (1998) additionally supplementing them using the abundances reported by Ferguson et al. (2005) in the low temperature regime.

For our nuclear network, we employ the MESA standard BASIC.NET network, which makes use of the nuclear reaction rates taken from JINA REACLIB Cyburt et al. (2010) employing additional tabulated weak reaction rates (Fuller et al. 1985; Oda et al. 1994; Langanke & Martínez-Pinedo 2000).

For our model atmosphere, we are making use of a varying Eddington-Grey atmosphere description (Eddington 1926). To model mass loss due to stellar winds, we employ the Reimers mass loss scheme (Reimers et al. 1975). We define the borders of the models convective and radiative zone via the Schwarzschild criterion Paxton et al. (2013) further enabling predictive mixing. We use the mixing length description provided by Henyey et al. (1965) and employ an exponential overshoot description (Herwig 2000) with an uniform overshoot parameter $f_0 = 0.005$ across all models. We calculate our models as non rotating stars.

According to the recommendation stated by Buchele (2025), we assume a value of $10^{-2}\,\mathrm{cm}^2/\mathrm{s}$ for OVERSHOOT_D_MIN. We furthermore make use of the improved routine presented by Buchele et al. (2026) to calculate $\Delta\Pi_1$.

A.2. Additional figures

In this Appendix, we present additional figures that complement the findings in our work. We provide a Hertzsprung-Russell diagram in Fig. A.1 showing the MESA model tracks of the representative stellar models listed in Tab. 1. We also provide a diagram showing the $\nu_{\max} - \mathcal{I}$ relation for the $M_{\mathrm{init}} = 1.0\,M_\odot$ mass-gain models in Fig. A.2, and the model density and magnetic sensitivity kernel profiles for the representative models listed in Tab. 1 in Fig. A.3 and Fig. A.4 respectively. We furthermore present the stellar radii and effective temperatures of the single-star and mass-gain models used in Sect. 3.2.1 and Sect. 3.2.2 in Tab. A.1.

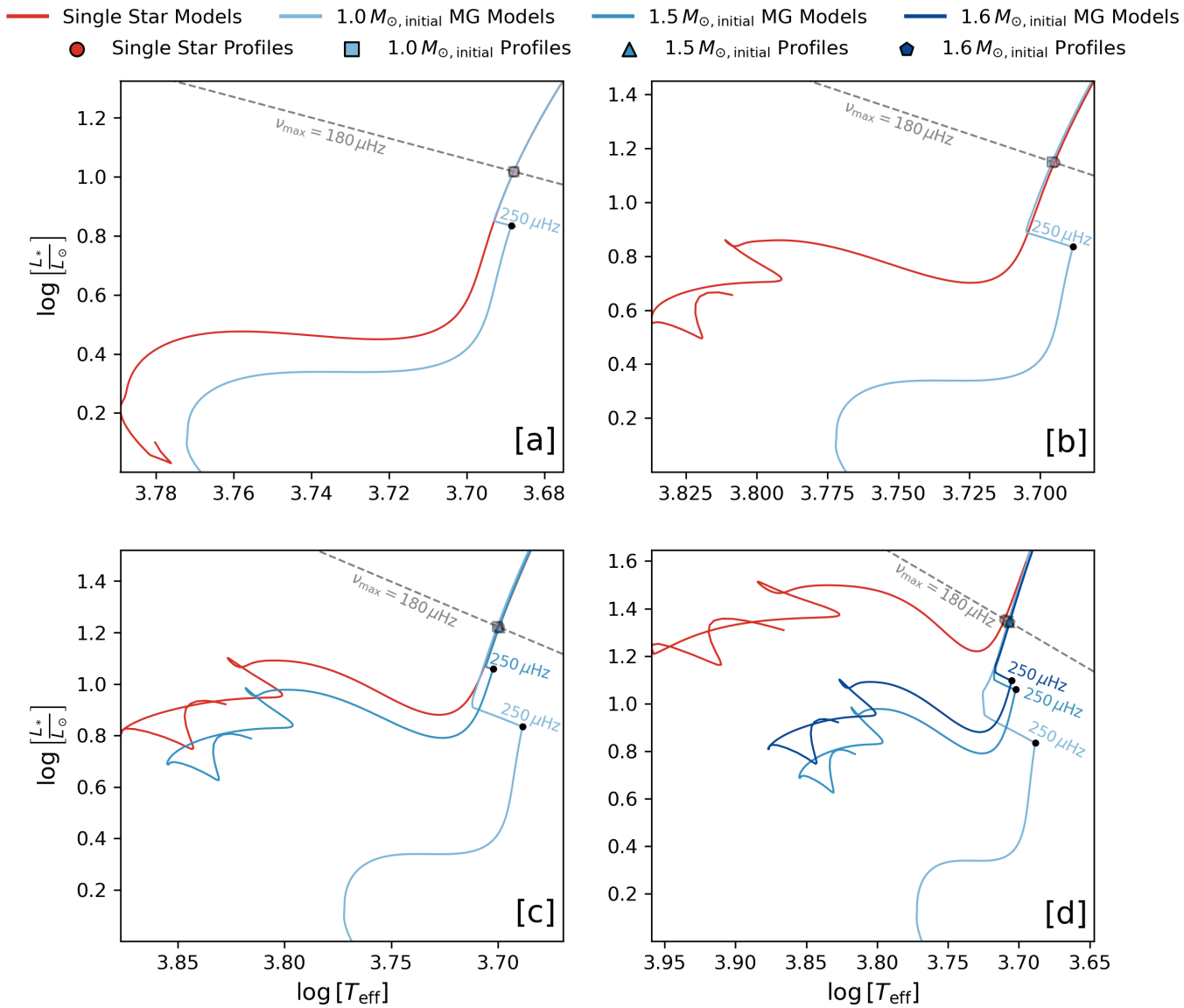


Fig. A.1. Evolutionary tracks for the representative single-star and mass-gain models, with the points in the HR diagram corresponding to the onset of the mass-gain event marked by model-specific symbols. The stellar models depicted in plot [*a*], [*b*], [*c*], and [*d*] possess a total (post-gain) mass of 1.1 $M_\odot$, 1.5 $M_\odot$, 1.6 $M_\odot$ and 2 $M_\odot$ respectively. The global power excess $\nu_{\max}$ is marked at a value of 180 μHz for all model tracks, making use of a rewritten form of the scaling relation introduced by Kjeldsen & Bedding (1995). The mass used to plot the tracks for $\nu_{\max}$ corresponds to the total (post-gain) mass of the models depicted in the respective panel.

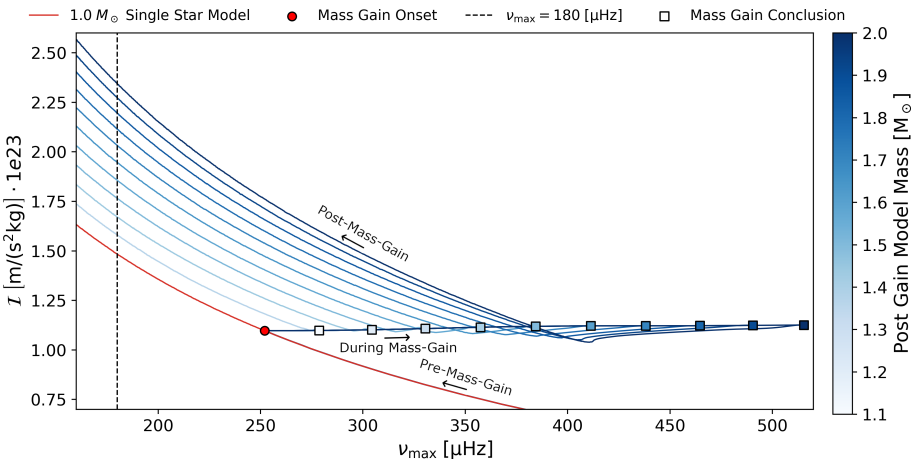


Fig. A.2. Relation between $\nu_{\max}$ and $\mathcal{I}$ for mass-gain models of initial mass 1.0 $M_\odot$ and post gain masses of $M_{\mathrm{total}} \in [1.1\,M_\odot, 2.0\,M_\odot]$ (blue model tracks) and a 1.0 $M_\odot$ single-star model. For the ease of the reader, the direction of evolution is marked by arrows that are labeled according to the evolutionary stage of the mass-gain models

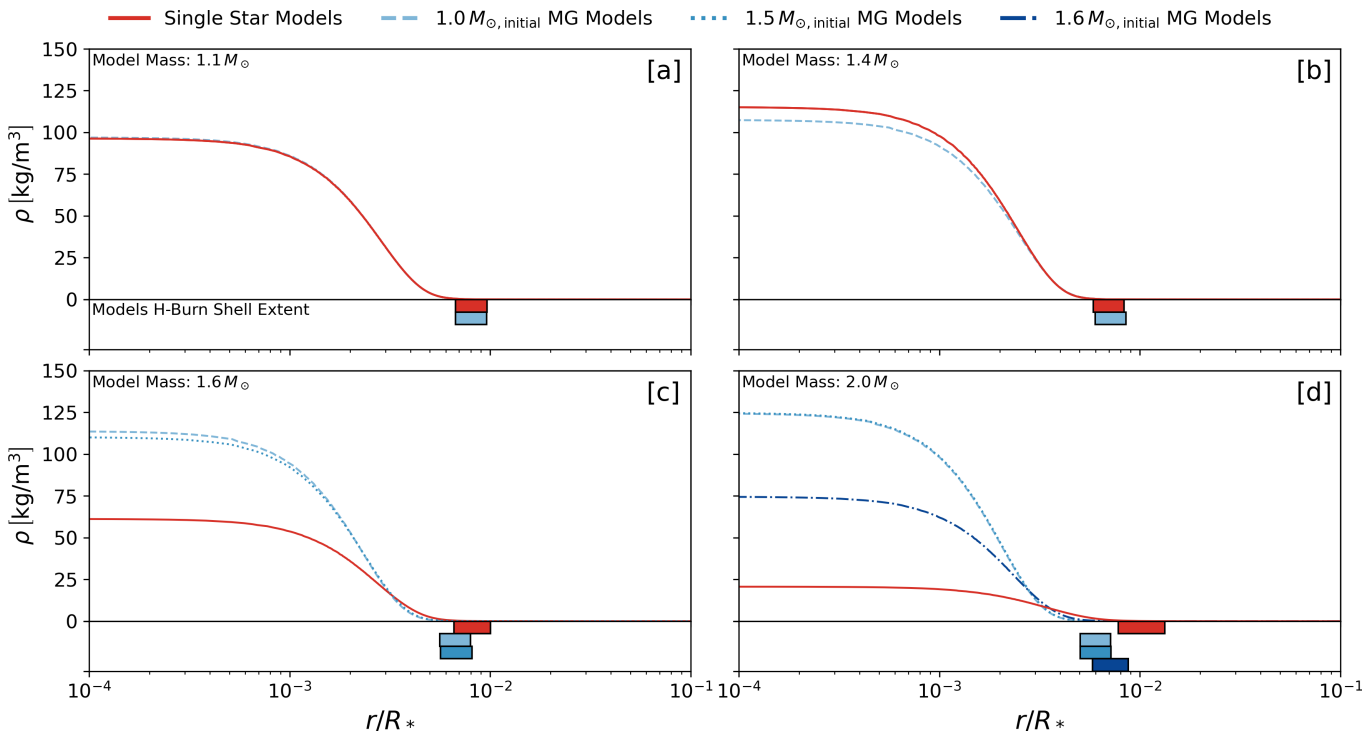


Fig. A.3. The model density ρ as well as the model-specific extent of the hydrogen burning shell obtained for the representative single-star and mass-gain models at a value for the frequency of the global power excess of $\nu_{\max} = 180\,\mu$Hz. The colored boxes at the bottom of each panel signify the extent of the hydrogen-burning shell of the respective single-star or mass-gain model. The labels [*a*], [*b*], [*c*], and [*d*] correspond to the model labeling introduced in Tab. 1.

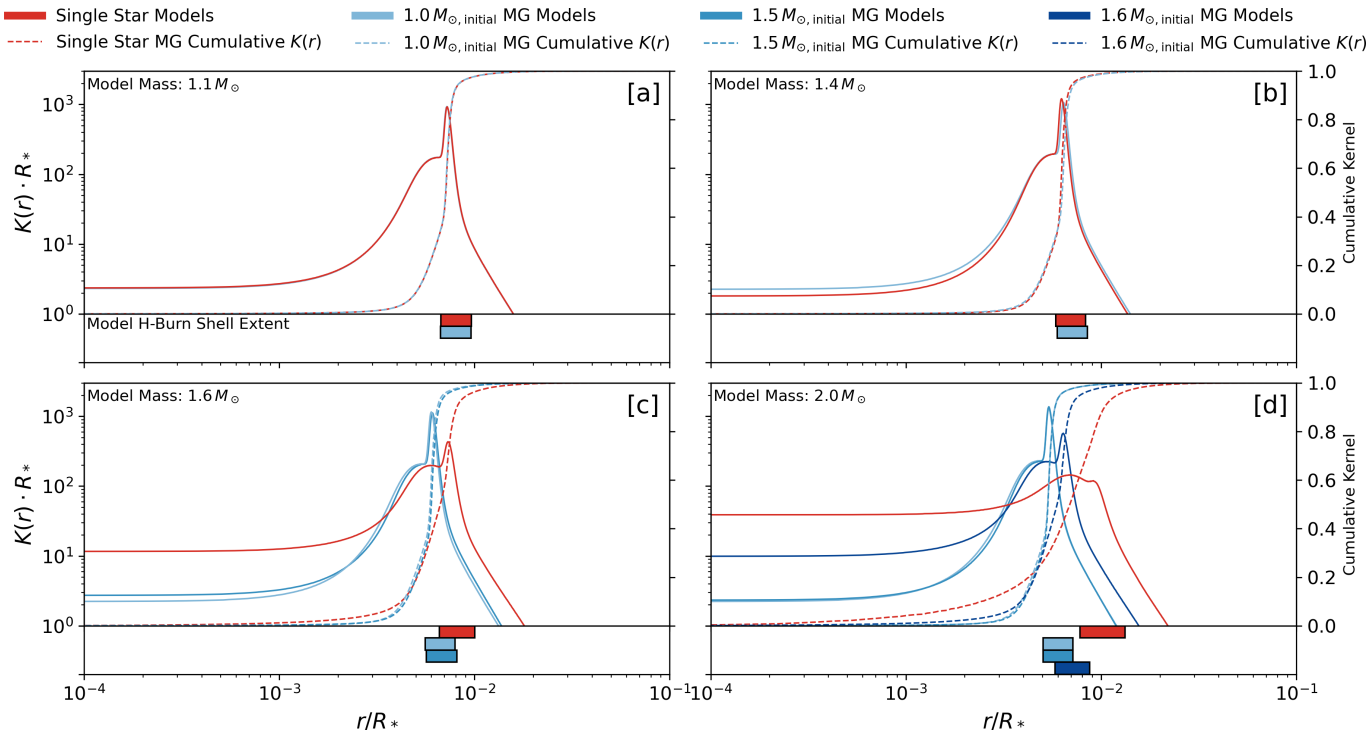


Fig. A.4. The magnetic kernel function K as well as the cumulative magnetic kernel function and the model specific extent of the hydrogen burning shell obtained for the representative single-star and mass-gain models. The labels [*a*], [*b*], [*c*], and [*d*] correspond to the model labeling introduced in Tab. 1.

Table A.1. Effective temperatures and stellar radii of our stellar models.

$M_{\rm total}$	Single		Mass-Gain ($M_{\rm init}$ = 1 $M_\odot$)		Mass-Gain ($M_{\rm init}$ = 1.5 $M_\odot$)		Mass-Gain ($M_{\rm init}$ = 1.6 $M_\odot$)	
[$M_\odot$]	$T_{\rm eff}$ [K]	R [$R_\odot$]	$T_{\rm eff}$ [K]	R [$R_\odot$]	$T_{\rm eff}$ [K]	R [$R_\odot$]	$T_{\rm eff}$ [K]	R [$R_\odot$]
1.0	4839	4.327	/	/	/	/	/	/
1.1	4874	4.530	4873	4.535	/	/	/	/
1.2	4900	4.724	4905	4.728	/	/	/	/
1.3	4928	4.914	4935	4.912	/	/	/	/
1.4	4954	5.093	4963	5.093	/	/	/	/
1.5	4980	5.263	4989	5.267	/	/	/	/
1.6	5006	5.428	5014	5.435	5004	5.435	/	/
1.7	5034	5.598	5037	5.592	5027	5.595	5027	5.595
1.8	5065	5.739	5059	5.749	5048	5.748	5048	5.754
1.9	5097	5.876	5079	5.900	5069	5.904	5067	5.906
2.0	5130	6.015	5099	6.048	5088	6.051	5086	6.056

Notes. The parameters provided correspond to the single star and mass-gain models used for our analysis in Sect. 3.2.1 and Sect. 3.2.2. The mass value in the $M_{\rm total}$ columns corresponds to the model mass in the case of the single-star models, and to the model mass after the mass-gain event in the case of the mass-gain models. All model parameters listed are taken at $\nu_{\rm max}$ = 180 μHz.